

THREE-DIMENSIONAL DYNAMICAL INSTABILITIES IN GALACTIC IONIZATION FRONTS

DANIEL J. WHALEN¹ & MICHAEL L. NORMAN²

Draft version November 12, 2017

ABSTRACT

Ionization front instabilities have long been of interest for their suspected role in a variety of phenomena in the galaxy, from the formation of bright rims and ‘elephant trunks’ in nebulae to triggered star formation in molecular clouds. Numerical treatments of these instabilities have historically been limited in both dimensionality and input physics, leaving important questions about their true evolution unanswered. We present the first three-dimensional radiation hydrodynamical calculations of both R-type and D-type ionization front instabilities in galactic environments (i.e., solar metallicity gas). Consistent with linear stability analyses of planar D-type fronts, our models exhibit many short-wavelength perturbations growing at early times that later evolve into fewer large-wavelength structures. The simulations demonstrate that both self-consistent radiative transfer and three-dimensional flow introduce significant morphological differences to unstable modes when compared to earlier two-dimensional approximate models. We find that the amplitude of the instabilities in the nonlinear regime is primarily determined by the efficiency of cooling within the shocked neutral shell. Strong radiative cooling leads to long, extended structures with pronounced clumping while weaker cooling leads to saturated modes that devolve into turbulent flows. These results suggest that expanding H II regions may either promote or provide turbulent support against the formation of later generations of stars, with potential consequences for star formation rates in the galaxy today.

Subject headings: H II regions: simulation—interstellar medium: ionization fronts—galaxy

1. INTRODUCTION

This is the first of two papers that study ionization front (I-front) instabilities in the nonlinear regime using three-dimensional radiation hydrodynamical simulations. In this paper we consider I-fronts propagating in a gas of solar metallicity, appropriate to galactic massive star forming environments. In a second paper, we simulate I-front propagation in primordial gas with low metallicities relevant to star formation at high redshifts. We demonstrate that the cooling properties of the gas have a large influence on how I-front instabilities manifest.

These instabilities have been the subject of numerous analytical and numerical studies for the past fifty years, primarily for their suspected role in the formation of inhomogeneities observed in galactic emission nebulae since the 1930’s (Kahn 1958; Axford 1964; Garcia-Segura & Franco 1996; Franco et al. 1998; Williams 1999, 2002). Initial corrugations in the fronts due to ambient density fluctuations are thought to elongate into ionized fingers extending ahead of the front that can evolve into the ‘elephant trunks’, bright rims, and cometary globules commonly seen in the galaxy today. Dynamical instabilities in H II regions are of direct relevance to the environments of massive stars (Freyer et al. 2003) and gamma-ray burst progenitors in general, possibly acting in concert with stellar winds to drive clumping of gas that later become susceptible to gravitational instabilities and collapse. Perturbations in the ionization front shocks of OB associations may also come into play

in scenarios of triggered star formation within molecular clouds (Dale et al. 2007). Historically, studies of I-front instabilities have progressed in both dimensionality and physics along two lines: unstable modes in R-type fronts and in D-type I-fronts (see Osterbrock (1989) for a review of modern I-front nomenclature and Whalen & Norman (2006) for numerical examples in one dimension).

1.1. Shadowing Instabilities in R-Type Fronts

R-type I-fronts propagate supersonically through media with minimal hydrodynamical coupling to the gas. The stability of this type of front to encounters with modest density perturbations was examined by Vandervoort (1962) and Newman & Axford (1967). Newman & Axford (1967) found the fronts to be weakly unstable but were unable to follow their evolution into D-type structures. Bertoldi (1989) studied the flash ionization of diffuse clumps in which the front does not revert to D-type (the ‘cloud-zapping regime’). He concluded that the clumps evaporate without forming new inhomogeneities in their wake but could not determine the downstream fate of the front itself. Several groups have investigated the shadowing of I-fronts by dense clumps (Mellema et al. 1998; Canto et al. 1998; Soker 1998), with particular focus on the evolution of the neutral tails behind the clumps. Most recent in this vein are the studies by Shapiro et al. (2004) of cosmological minihalo photoevaporation by external Population III and quasar ionizing sources at high and intermediate redshifts. The aim of these simulations was to assess the role of minihalos as sinks of ionizing UV photons during cosmological reionization. Shadows rather than instabilities arose in these models because the obstructions trapped the I-fronts as they evaporated.

¹ Applied Theoretical Physics (X-2), Los Alamos National Laboratory

² Center for Astrophysics and Space Sciences, University of California at San Diego, La Jolla, CA 92093, U.S.A. Email: dwhalen@cosmos.ucsd.edu

Williams (1999) revisited instability modes in R-type fronts, in this instance following their transition to D-type far downstream of the original perturbation. Their analysis revealed that the overdensity indents a planar R-type front with a dimple that first elongates but then saturates (Fig 1 in Williams (1999)). The ionizing photons are oblique to the sides of the dimple but incident to its tip. Since the flux is lower at the sides than at the tip, as the front approaches the Strömgren position the shock breaks through the front along the wall of the dimple before its tip. Still R-type, the tip races forward, elongating the dimple into a nonlinear jet instability when the transition to D-critical is complete. If the shocked gas efficiently cools, the thin-shell hydrodynamic instability appears and fragments the gas into clumps with densities hundreds of times greater than the ambient medium.

1.2. Dynamical Instabilities in D-Type Fronts

D-type I-fronts move supersonically with respect to the upstream neutral gas, but subsonically (or sonically) with respect to the downstream ionized gas. Consequently, D-type fronts are preceded by shocks in the neutral gas. Soon after the modern nomenclature for I-fronts was established, Kahn (1958) and Axford (1964) examined the stability of perturbations in planar weak D-type fronts. They discovered that recombinations to the ground state within ionized fingers advancing ahead of the front effectively dampened their further growth upon reaching lengths of a few n_i^{-1} pc, where n_i is the electron density in the postfront gas. This is the product of the sound speed of the ionized gas and its recombination time; in galactic environments such corrugations are initially short wavelength and saturate quickly. As the fingers lengthen, photons must cross more neutrals resulting from recombinations, which attenuate the ionizing flux advancing the tip of the disturbance.

Instabilities that do exhibit strong growth were later discovered in D-type ionization fronts, but only in conjunction with pre-existing flow instabilities (Vishniac 1983; Capriotti 1973; Brand 1981). In general, expanding spherical shocks are prone to a variety of dynamical instabilities that can result in their fragmentation and breakup. Radiating shocks are subject to the Vishniac (or thin-shell) instability in either uniform densities or gradients, while Rayleigh-Taylor instabilities can arise in adiabatic or radiating flows if they accelerate (which occurs in radial power-law density gradients steeper than r^{-2}).

The Vishniac mechanism can be visualized as follows (Fig 1 of Mac Low & Norman (1993)): in the frame of the shock, the inflow ram pressure is unidirectional while the ionized postshock pressure is isotropic. If a density fluctuation is advected across the shock, small transverse velocities arise across the face of the shock that create overdensities and underdensities along adjacent lines of sight from the center of the shell. The postshock gas then protrudes through the underdense regions, dimpling the shock into peaks and valleys and forcing even greater transverse flows that further bunch gas across adjoining lines of sight. However, the higher pressures in the troughs eventually reverse the transverse flows, resulting in oscillatory ripples with modest growth rates across the face of the shock commonly known as overstabilities.

Both thin-shell overstabilities and Rayleigh-Taylor in-

stabilities are exacerbated when driven by an ionization front (Spitzer 1954; Frieman 1954; Giuliani 1979; Garcia-Segura & Franco 1996; Williams et al. 2000; Mizuta et al. 2005, 2006). When perturbations appear in the shell, the radiation preferentially advances into the lower optical depths of the underdensities, reinforcing the transverse velocity gradients that originally created them in a repeat of the cycle described above (Fig 1 of Garcia-Segura & Franco). What distinguishes unstable modes in blast waves or wind-blown bubbles from those in D-type fronts is their amplitude: in extreme cases the radiation may escape through cracks in the shock, driving even greater hydrodynamical growth (Garcia-Segura & Franco 1996; Franco et al. 1998; Freyer et al. 2003). The violence of flow instabilities in general is largely governed by the cooling rates of the shocked gas. Efficient cooling collapses the shocked neutral gas into a thin, dense cold shell more prone to breakup than a thick semi-adiabatic shock. We note that a class of long-wavelength unstable surface modes in weak D-type fronts has recently been uncovered by analytical and numerical work done by Sysoev (1997) and Williams (2002) that are independent of any other flow instabilities, but we do not consider them here.

A key question is how the dimensionality of ionized flows dictates the nature of perturbation growth in R-type and D-type fronts, given that published simulations have been confined to two dimensions. Furthermore, instability growth is mediated by I-front transitions in prefront shocked gas that mandate radiation hydrodynamics rather than the approximations heretofore performed (Garcia-Segura & Franco 1996; Dale et al. 2007; Yoshida et al. 2006). In order to explore these issues we have performed the first three-dimensional radiation hydrodynamical calculations of dynamical instabilities in D-type fronts (Franco et al. 1998) and shadowing instabilities in R-type fronts (Williams 1999) with metal-line cooling. These models have been made possible by recent upgrades to the ZEUS-MP reactive flow physics code (Whalen & Norman 2006) (hereafter WN06) to perform fully-parallelized three-dimensional radiation transport for a point source in spherical polar grids and for plane waves in cartesian boxes. Our calculations are intended to survey the qualitative nature of three-dimensional instabilities in galactic ionization fronts rather than provide detailed comparisons to analytical studies, which have only been performed in one dimension. We focus on dynamical phenomena in r^{-2} density fields for comparison to earlier two-dimensional numerical work and for their similarity to clump profiles observed in massive star forming regions within molecular clouds in the galaxy today (Arquilla & Goldsmith 1985; Gregorio Hetem et al. 1988). Our numerical suite is therefore of direct relevance to the environments of massive stars as well as the morphologies of emission nebulae in the interstellar medium (ISM). Since our simulations all employ radiative cooling in uniform or r^{-2} densities, we expect initial perturbation growth to be dominated by Vishniac modes. In nearly adiabatic primordial gas with steeper gradients such as those in cosmological minihalos, unstable modes could be initiated through the Rayleigh-Taylor channel, a possibility we investigate in a following paper.

In Section 2 we describe the improvements to our ra-

diative transfer and reaction network integration scheme required by transport in three dimensions as well as the parallelization and load balancing of the transport itself. In section 3 we compare two-dimensional calculations of dynamical instabilities on polar grids performed with simplified ionization equilibrium physics to those with full radiative transfer. Our three-dimensional simulations of these instabilities on spherical-polar coordinate grids are detailed in Section 4 and we present three-dimensional calculations of the shadow instability Williams (1999) in section 5. Implications of this work are discussed in Section 6.

2. ZEUS-MP ALGORITHM UPGRADES

The ZEUS-MP hydrocode utilized in previous one-dimensional work (Whalen *et al.* 2004) is now fully parallelized for three-dimensional applications. We implemented the transport of UV plane waves along the x-axis of a cartesian box (or along the z-axis of a cylindrical coordinate grid) in addition to the original radial transfer of photons from a point source centered in a spherical polar coordinate mesh. The parallel reactive flow, additions to the radiative transfer, and improvements to our subcycling scheme are detailed below.

2.1. Parallelization Scheme

We refer the reader to WN06 for a description of our sequential multistep radiation algorithm. ZEUS-MP decomposes the simulation domain into subunits called tiles, with each tile assigned to a single processor for the duration of a calculation (Hayes *et al.* 2006). Global solution concurrency is maintained by message-passing between processors through calls to the Message Passing Interface (MPI) library. In general, the computational domain can be partitioned along all three axes but in photoionization calculations we limit the decomposition to two axes only. In cartesian coordinates we subdivide the volume along the y and z directions only; in cylindrical coordinates the decomposition is along the r and phi axes, and in spherical grids we tile only along theta and phi. Hence, a tile in a cartesian grid is a rectangular box whose length in the x direction spans the entire grid. In cylindrical coordinates, tiles are wedges in r and phi lengthwise in z, and in spherical coordinates they are slices in theta and phi radiating outward from the coordinate center to the outer radial boundary.

Domain decomposition is implemented along only two coordinates in ZEUS-MP to enforce load balancing of the radiative transfer and to avoid the need to communicate photon fluxes between adjacent tiles. The key to effective load balancing is requiring that the ionization front be present in all the tiles at once. Subdivision along all three axes for a single point source or plane wave would result in the few tiles hosting the front shouldering a disproportionate fraction of the chemistry subcycling, leaving the other tiles relatively idle. The tradeoff in this scheme is the limit to the parallelization that can be applied to a given problem.

The reaction network is evolved plane by plane within a tile. Updates to the reaction network can be made one plane of zones at a time because the chemistry in any given zone over Δt_{chem} does not depend on its nearest neighbors. We advance the network one plane at a

time so the reaction coefficients can be stored in two-dimensional arrays. Up to thirty rate coefficients are present in the reaction network and as many as 21 heating and cooling coefficients comprise the isochoric update to the gas energy. Any network update order requiring the coefficient arrays to be three-dimensional would inflate the memory required for a calculation by a factor of ten beyond what is required just for hydrodynamics.

We prevent the solution for the entire grid from being evolved further than the shortest evolution time in any of its tiles by performing an MPI all_reduce operation to extract the global minimum of Δt_{heat} . The smaller of the grid minima of Δt_{heat} and the Courant time is adopted for the hydrodynamical update of gas energies, densities, and velocities. To further preserve solution coherence, mpi_barrier calls are stationed at the end of the reaction network module to ensure subcycling is complete in all the tiles before any of them advance to the next operator-split step in the hydrodynamics. This procedure is necessary because of the implementation of asynchronous message passing in ZEUS-MP, in which code execution in some tiles can proceed while communication between other tiles is still in progress.

2.2. Radiative Transfer: Cartesian and Cylindrical Coordinates

We compute the attenuation of the ionizing flux along rays parallel to the grid lines. In cartesian coordinates, the rays are parallel to the x-axis. In cylindrical coordinates, the rays are parallel to the z-axis. Generalizing the radiative rate coefficients k_{rad} evaluated in WN06 to planar radiation flows is straightforward. Recalling that the number of photons removed from a zone per second (n_{ioniz}) is related to the radiative rate coefficient (k_{rad}) by eq. 18 of WN06

$$k_{rad} = \frac{n_{ioniz}}{n_H V_{cell}}, \quad (1)$$

and that photon conservation demands that

$$n_{ioniz} = \frac{F_{out}A_{out} - F_{in}A_{in}}{h\nu}, \quad (2)$$

where F and A are the flux (in erg/sec/cm²) and area over the given face of the zone, we have that

$$k_{rad} = \frac{\dot{n}_{ph} (1 - e^{-\chi(r_{i+1}-r_i)})}{n_H \Delta x}, \quad (3)$$

where \dot{n}_{ph} is the emission rate of all photons at a given energy, Δx is the zone length along the x-axis, and χ is the mean free path of the photons in the neutral gas. This derivation holds with axial plane wave transport in cylindrical geometries because the metric terms in the area factors drop out. We include an option for attenuating the plane wave flux by r^{-2} to approximate the geometric dilution of a point source.

We tested the radiative transfer by computing the position of a one-dimensional planar ionization front in a uniform static medium of hydrogen, with $n_H = 1000 \text{ cm}^{-3}$ and $T = 72 \text{ K}$. The grid has 1000 zones in the x direction and a length of 1.0 pc. The photon flux along the x-axis

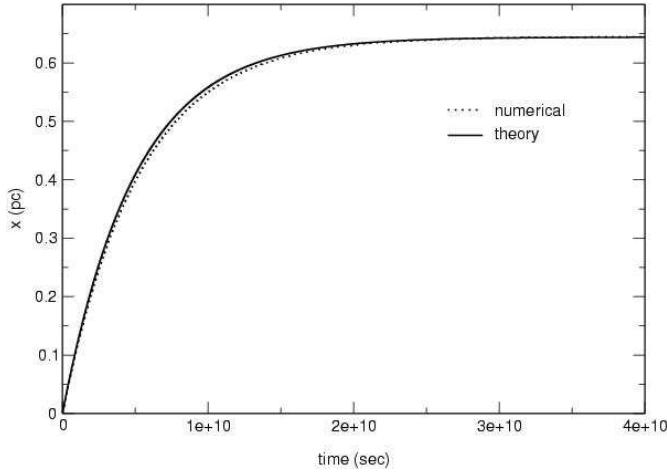


FIG. 1.— Approach of the static planar ionization front to x_{Str} , numerical vs analytical.

incident to the left-hand face is $J_0 = 4.0 \times 10^{11} \text{ cm}^{-2} \text{ s}^{-1}$, and we applied a constant case B recombination coefficient $\alpha_B = 2.015 \times 10^{-13} \text{ cm}^3 \text{ s}^{-1}$. By equating the photon flux at the front to the incoming flux of neutral particles we can compute the velocity and position of the front in the usual manner:

$$v_f = \frac{m_i}{\rho_i} J_f = \frac{n_{\gamma,f}}{nA} = \frac{1}{n} [J_0 - x_f n^2 \alpha_B] \quad (4)$$

where $n_{\gamma,f}$ is the total number of ionizing photons reaching the front per unit time and A is the area of the zone face. The position of the front easily follows from simple integration:

$$x_f = \frac{J_0}{n^2 \alpha_B} (1 - e^{-\alpha_B t}) \quad (5)$$

We show the evolution of the front in the static medium in Fig 1; for the parameters of this test, $x_{Str} = 0.644 \text{ pc}$. The code agrees with the analytical prediction to within 5% at all times. A parallelized version of this test was performed in three dimensions to verify that the advance of the front in each tile was identical.

2.3. Advanced Subcycling

As detailed in WN06, in one-dimensional problems the primordial gas reaction network in ZEUS-MP was cycled over consecutive chemical timesteps

$$\Delta t_{chem} = 0.1 \frac{n_e}{\dot{n}_e} \quad (6)$$

until a hydro timestep was covered

$$\Delta t_{hydro} = \min(\Delta t_{cour}, \Delta t_{heat}) = \min\left(\frac{\Delta r}{c_s}, 0.1 \frac{e_{gas}}{\dot{e}_{ht/cl}}\right) \quad (7)$$

This scheme proved to be robust and versatile, accommodating regions experiencing either photoionization or recombination. However, timescale analysis revealed that

cells close to the source without any initial electron fraction required as many as 70 - 80 hydrodynamical updates before coming to ionization equilibrium upon arrival of the front. Network subcycling between updates also tended to be extreme in such zones, with several thousand iterations required to cross Δt_{hydro} at times, far more than are required for accuracy. The problem is ameliorated at larger radii because heating times increase further away from the source. Also, advection transports small electron fractions into zones slightly ahead of the front, preventing initially minute Δt_{chem} .

Practical I-front transport in three dimensions required two improvements to our integration scheme. When the front encounters overdensities, advection of electrons into those zones is halted, resulting in paralyzingly short chemical timesteps until the front exits the perturbation. We eliminated this problem by modifying Δt_{chem} :

$$\Delta t_{chem} = 0.1 \frac{n_e + 0.001 n_H}{\dot{n}_e} \quad (8)$$

The correction term ensures that Δt_{chem} is not too small when photoionizations commence in the zone and has little effect as the zone approaches equilibrium and Δt_{chem} increases. The algorithm now advances ionization fronts through density jumps without difficulty.

We also experimented with more aggressive subcycling by requiring that a zone come to ionization equilibrium in no more than 7 - 8 hydrodynamical updates by altering Δt_{hydro} :

$$\Delta t_{hydro} = \min\left(\Delta t_{cour}, \frac{e_{gas}}{\dot{e}_{ht/cl}}\right). \quad (9)$$

We obtain speedups of up to 15 in transporting R-type fronts with this time step prescription, but there is little improvement with D-type fronts because in primordial environments Δt_{cour} is usually the smaller of the two timescales in eq. 9. Two difficulties arose in this method. First, the longer time step can cause overshoot in the cooling as the zone reaches full ionization, occasionally removing all the gas energy in a zone in a single update. We resolved this issue by reverting to the original time step if $\dot{e}_{gas} < 0$ in a zone, which removed the anomalous cooling with little sacrifice in performance.

Unfortunately, the coarser time steps can lead to inaccuracies in the reaction network, causing the propagation of R-type fronts to diverge from theory by as much as 10 - 20%. In many practical applications this is not a serious error, so the performance gain may outweigh the loss in accuracy. While we retain both subcycle options in the code, we applied only the improved Δt_{chem} to these studies to properly capture perturbations in R-type fronts that later grow into instabilities after becoming D-type.

3. D-TYPE INSTABILITIES IN TWO DIMENSIONS

We now examine the growth of unstable modes in a D-type ionization front that is expanding in a radially symmetric gas profile randomly seeded with minute fluctuations in density on a polar coordinate grid. We consider the development of instabilities in a uniform core

enclosed by an r^{-2} envelope

$$n_H(r) = \begin{cases} n_c & \text{if } r \leq r_c \\ n_c(r/r_c)^{-2} & \text{if } r \geq r_c \end{cases}$$

assuming that the shocked gas is radiatively cooled by metal emission lines. This problem was first studied by Garcia-Segura & Franco (1996) (hereafter GSF) and we compare their results below.

We augmented the isochoric gas energy update in ZEUS-MP (eq. 9 of WN06) with cooling curves from Dalgarno & McCray (1972) in which any elemental abundances can be specified. The Dalgarno & McCray curves include both electron and neutral hydrogen collisional excitation of H, He, and neutral and singly-ionized C, O, N, Fe, Si, and S. The energy equation also has cooling due to electron collisional ionization of hydrogen, H and He recombinational cooling, bremsstrahlung cooling, and Compton cooling by free electrons off the cosmic microwave background (for high-redshift applications). These latter two processes play a negligible role in our simulations. In general, the Dalgarno & McCray cooling rates in a given cell can be constructed with any electron or neutral H number density derived from the reaction network. For consistency with GSF, we evaluate them assuming a fixed electron fraction of 0.01 and solar metallicity in the calculations in this paper, regardless of the true electron abundances on the grid.

This treatment approximates radiative cooling in shocked neutral gas well but underestimates metal line cooling, H- α cooling, and He- α cooling in ionized gas because the electron fraction is much higher than 0.01 there. At postfront gas temperatures above $\sim 10^4$ K, H- α and He- α cooling rates per atom can exceed those of the metals by four orders of magnitude. Given that neutral H and metal fractions in the ionized gas at solar metallicities are roughly equal ($\sim 10^{-5}$), H- α and He- α cooling dominates the total Dalgarno & McCray curve inside the H II region. However, in the pure H simulations of this study we incur overestimates of at most 10% in temperature in the ionized gas because it is H recombinational cooling that really controls postfront temperatures, as we demonstrate below. Cutoff temperatures were also incorporated in the runs, defined to be the gas temperature below which cooling is not applied to the gas energy density. For the two runs discussed in this section we adopted cutoff and background of temperatures of 100 K.

A point source of ionizing UV flux was centered on the polar coordinate grid with 200 radial zones and 180 zones in the theta direction. The inner and outer radial boundaries were 0.01 pc and 2.0 pc with reflecting and outflow boundary conditions, respectively. The inner and outer boundaries in the theta direction were $\pi/4$ and $3\pi/4$, respectively, with reflecting boundary conditions. We adopted this angle range to avoid the minute Courant times associated with zones near the coordinate poles due to their small angular dimensions. At the resolution of this simulation we obtain minimum Courant times ten times greater over this range than at the poles. Our choice of reflecting boundary conditions could exclude the growth of long-wavelength modes, but the linear stability analysis of Giuliani (1979) predicts that short-wavelength modes will initially dominate and then

later consolidate into larger structures.

The density profile in both runs was hydrogen only, with a flat central core of $1.0 \times 10^4 \text{ cm}^{-3}$ out to $r = 0.2$ pc followed by an r^{-2} dropoff. At the outer boundary the density falls to $\sim 100 \text{ cm}^{-3}$. The initial gas temperature was set to 100 K. We adopted a photon emission rate \dot{n}_{ph} of $1.0 \times 10^{48} \text{ s}^{-1}$ with energy 15.2 eV, with an energy per ionization ϵ_I of 1.6 eV in order to maintain the ionized gas temperature at 1.0×10^4 K. Theory predicts that if the initial Strömgen radius falls in the density gradient the I-front will revert from D-type to R-type and overrun the envelope (Franco *et al.* 1990). For the central density and emission rate of these runs, the Strömgen radius

$$R_S = \left(\frac{3\dot{n}_{ph}}{4\pi\alpha_B n_c^2} \right)^{1/3} \quad (10)$$

is 0.065 pc, entirely within the central core. The transition to R-type is thus delayed.

In the first run we do not perform radiative transfer but instead repeat the simplified treatment applied in the GSF models. Every hydrodynamical time step the equilibrium position of the I-front is computed along a given radial ray by equating the sum of the case B recombinations along the ray to the emission rate of the central source:

$$\int_0^{r_f} 4\pi r^2 n_e n_p \alpha_B dr = \dot{n}_{ph} \quad (11)$$

The gas temperature is then set to 1.0×10^4 K along the line of sight out to r_f . After repeating this procedure for every value of theta the model is evolved for a Courant time. The position of the front thus changes each time step as gas is rearranged on the grid by the high-temperature flow. We refer to this approach in the following as “ionization equilibrium”. In practice, we found it necessary to limit the cooling in a shocked zone to be no greater than 90% of the energy remaining in the zone above the temperature cutoff of the cooling curve. Otherwise, the rather coarse hydrodynamical timesteps can allow explicit updates to the energy equation to completely remove all energy within the cell. No R-type fronts ever arise in this approximation since the fronts by construction are always assumed to have reached the Strömgen at any given time step.

In the second run we transport the front across the grid using radiative transfer scheme described in Sec. 2.2, coupled to self-consistent photoionization and heating as described in Sec. 2.3 (see also WN06). In the Garcia-Segura & Franco (1996) simulations, density fluctuations with randomly-distributed amplitudes of at most 1% were imposed on very zone to seed the formation of shock instabilities. We also did this, holding the gas energy density constant to prevent pressure fluctuations from dispersing the perturbations. However, in our model we only imposed these variations beyond radii of 0.125 pc to prevent the onset of shadowing instabilities in the early R-type front before dynamical instabilities in the D-type front can form. We compare the evolution of both models in Fig 2.

3.1. Ionization Equilibrium vs Radiation Hydrodynamics

Both models confirm the prediction of Giuliani (1979) that the modes which grow fastest are those with the largest wavelengths. Unstable modes begin to disrupt the shock at 9.5 kyr in the second run, with 13 spikes visible at 28.5 kyr (panel (b)) but only 5 remaining at 148.4 kyr (panel(f)). Vorticity in the flow is evident where the bases of the spikes join the flared regions. The instabilities remain D-type: they are always bounded by a dense shocked gas layer and their ionized interiors have time to laterally expand as they elongate. The perturbation amplitudes never saturate in either model but continue to grow well into the nonlinear phase, from 0.1 pc at 28.5 kyr to 0.5 - 1.0 pc at 148.4 kyr in the second run. Direct quantification of their growth rates is problematic because individual structures coalesce over time, but their rapid elongation at later times is due to their descent down the density gradient.

There are noticeable differences in structure of the fronts at early and intermediate times. While the ionized fingers are numerous and narrow in both simulations at early times (panels (a) and (b) of Fig 2), their morphologies diverge after a few tens of kyr. Ionized spikes push past each other at random times through the shock in the second run, flaring sideways earlier than in the first run because they are not as collimated by their neighbors. In contrast, the spikes advance nearly in step with one another in the first model, remaining cylindrical out to much greater distances because of the parallel advance of their neighbors. There are also less of them: 7 spikes at 0.3 pc in comparison to 13 in the second simulation. The differences between the two models are most pronounced at early and intermediate times, becoming less distinct as they enter highly nonlinear regimes.

The departures are chiefly due to how the two numerical schemes capture the interaction of the front with the shocked neutral shell. The topology of the instability is sensitive to how the inner shell is photoevaporated. Ionization equilibrium abruptly assigns temperatures of 1×10^4 K to the fluid elements on the inner surface that are capable of being ionized. Had they instead been incrementally heated and ablated, as in the radiation hydrodynamical scheme, their subsequent expansion would have created a larger number of cracks in the shell distributed over time, yielding the larger number of ionized fingers observed in the second run. Although costlier, full radiation transport is necessary to model the actual deformation of the shocked shell. Initial disparities in the deformation of the shell by the two algorithms lead to the much greater differences in morphology at intermediate times evident in panels (c) and (d) of Fig 2.

In one-dimensional calculations the two algorithms predict I-front positions to within a few percent of each other at early times but diverge by more than 10% at later times, as shown in Fig 3. This agreement holds only so long as the front is D-type. Ionization equilibrium approximations would not fare as well if the front became D-type in the r^{-2} gradient or in other stratified media. It would fail altogether if the front executes transitions from D-type to R-type or vice versa, as is common in cosmological H II regions. We have found that updates to velocities should be performed on photoheating time

scales rather than the Courant time to capture the true acceleration of fluid elements by the front in power-law density gradients (WN06).

4. THREE-DIMENSIONAL D-TYPE INSTABILITIES

We extended the radiative transfer calculation in section 3 to three dimensions using a spherical polar coordinate grid with 200 radial zones and 180 zones in the theta and phi directions. The inner and outer radial boundaries were again 0.01 pc and 2.0 pc with reflecting and outflow boundary conditions, respectively. The angle boundaries were again chosen to be $\pi/4$ and $3\pi/4$ in phi and theta with reflecting boundary conditions. We apply the same randomly perturbed density profile as before to the grid, with the energy per ionization ϵ_I set to 1.6 eV to ensure a postfront gas temperature of 1.0×10^4 K.

Our first run (S31) had cutoff and background temperatures of 1000 K and 10 K, respectively, while our second run (S22) had cutoff and background temperatures of 100 K. Metal lines cannot fully cool shocked gas in the first case so the shell is thinner than in an adiabatic flow but not as dense (or cold) as when the metals are free to cool the gas down to the background temperature. Garcia-Segura & Franco (1996) nevertheless found instabilities to readily form in these circumstances in their two-dimensional simulations. The lower cutoff in the second run is intended to produce a relatively cold, dense shell that will break up more violently. In both of these models \dot{n}_{ph} was again chosen to be $1.0 \times 10^{48} \text{ s}^{-1}$ so that the Strömgren sphere would reside within the core.

4.1. S31 Instability

In Fig (4) we show $\phi = \pi/2$ slices of the evolution of the ionization front in the S31 run at 29.5 kyr, 70 kyr, and 100 kyr (the total time for which the front was followed in the 1996 experiments). In panels (a) and (b) the perturbations are seen to be dominated by short-wavelength modes at early times that later merge into the longer-wavelength modes in panels (c) and (d), in accord with linear stability analysis. The initial wavelengths are of the order of the shell thickness. Unable to completely cool, the shocked shell becomes thicker as neutral gas accumulates onto it, acquiring turbulent motions as it evolves. The instabilities persist to 200 kyr in these three-dimensional calculations as seen in panels (e) and (f) but saturate without the prominent growth exhibited in the GSF two-dimensional models. The turbulence in the shell appears to prevent the unstable modes from breaking out. The maximum density attained by the clumps in the course of the simulation is $4.99 \times 10^4 \text{ cm}^{-3}$; pronounced clumping is visible at 177 kyr in panel (f).

4.2. S22 Instability

The ionization front breaks through the shock and escapes much further down the stratified envelope in the S22 run, as dramatically illustrated in Fig (5). We show $\phi = \pi/2$ slices of the front for this model at 20.8 kyr, 67.9 kyr, and 124.5 kyr. Radiation flares outward through the cracks in this more violently fragmenting, colder, denser shell, and the dominant growth modes over time

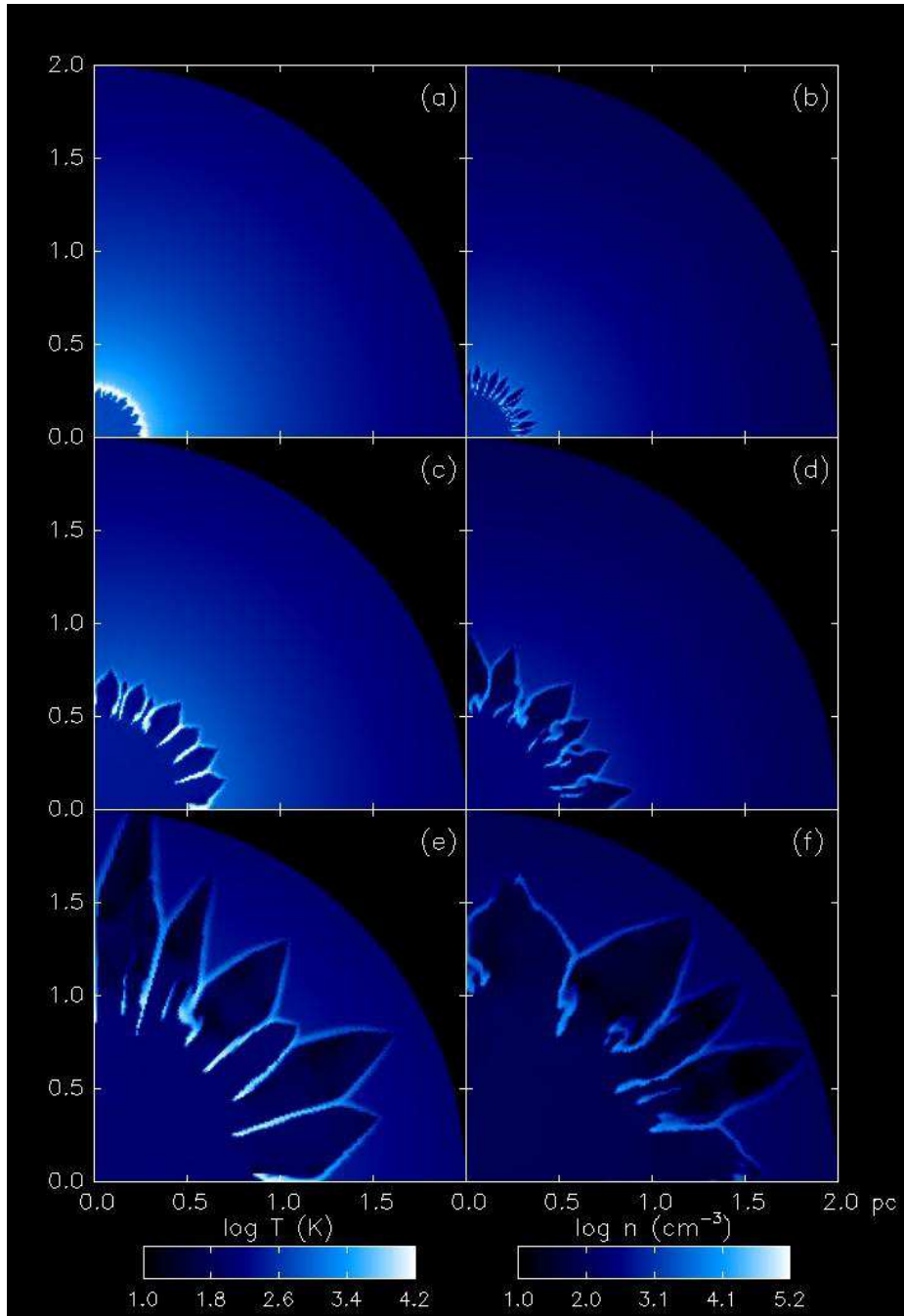


FIG. 2.— Dynamical instability in a D-type I-front propagating out of an r^{-2} density gradient with metal line cooling. Panels (a), (c), and (e): number densities at 28.5 kyr, 76.1 kyr, and 148.4 kyr for a front evolved assuming simple ionization equilibrium. Panels (b), (d), and (f): density evolution of an I-front transported across the grid with full radiative transfer at 28.5 kyr, 76.1 kyr, and 148.4 kyr.

are again those with the greatest wavelengths. This motion is visible in the large dark neutral patches cutting across some of the ionized flares in temperature panel (e) of Fig (5). Comparison of panels (c) and (e) demonstrate the transience of these features. Newly ionized gas in the outer regions of the flares expand laterally as the instabilities propagate, creating dark, rarefied zones in the corresponding density panels. The unstable modes advance as D-type, given their time scales of expansion as well as because they remain bounded by shocked gas that is visible as a thin, lighter hued density layer in the outer

edges of the flares. The maximum density of the gas in this run is $2.08 \times 10^5 \text{ cm}^{-3}$, greater than in the previous run due to the higher degree of postshock cooling. The thin radial segments of cool zones visible in temperature panels (c) and (e) are cold, dense shell fragments of the shocked shell not yet ionized by the front. These fragments can be seen to originate in the cold shell because they extend from the base of the instabilities and radiate outward. They are overtaken on either side by hot ionized outflows, with the neutral parcels of gas closest to the central source eventually becoming ionized them-

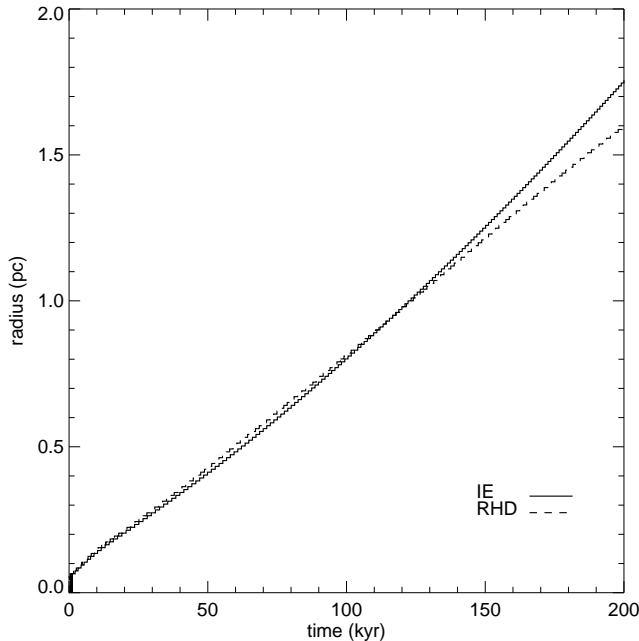


FIG. 3.— One-dimensional I-front positions in the ionization equilibrium approximation and with radiative transfer

selves. Their large densities stand out in relief against the surrounding dimmer regions in panels (d) and (f). The cooling of the fragments down to the cutoff temperature is due their high densities rather than some instability in the explicit updates to the energy equation. Our integration scheme prevents any energy loss greater than 10% over the time step on which hydrodynamic updates are performed. Large clumps of gas can be seen to persist to late times as they are blown outward by the front in panel (f).

There are clear qualitative differences between the unstable flow in the two-dimensional radiation hydrodynamical model in the last section and this run that can only be attributed to their dimensionality, given that both otherwise employ the same physics. First, transverse flow of gas into the plane of the image from above and below is evident in some of the dark patches in the outer regions of the ionized fingers in panels (c) and (e). These are not cold dense shell fragments (as the density panels attest) but instead are neutral gas crowded into the plane of the image by adjacent instabilities. Second, the shapes of the fingers differ in the two runs: the structures in the three-dimensional model are both more narrow and plentiful than in the two-dimensional run. Less flaring occurs in the three-dimensional fingers because they are partially collimated by neighboring flows that are not possible in the two-dimensional models. The geometry of cracks in the shell at the base of the instabilities may also be altered by the additional degree of freedom in the flow.

The S31 and S22 data confirm that I-front breakout from the envelope is determined by both the degree of fragmentation of the shell (which is governed by the efficiency of cooling in the shocked gas) and the pressure ratio of the ionized and background gas. At early stages of the instability there are clear differences in the initial

scales of the perturbations that we suspect, but have not confirmed, are due the thickness of the shocked gas shell at the time of initial fragmentation. The shell thicknesses vary from five to ten zones at early times, within the numerical resolution of our mesh. The initial scales of these deformities in part differentiate the later topologies of the S31 and S22 instabilities.

We further note that the absence of runaway instabilities in our S31 model may in part be due to R_S being less than r_c . In one dimension, somewhat surprisingly we find that the density envelope actually confines the front behind the shock at distances far beyond the problem boundaries in our calculations, in contrast to the relatively quick breakout that would occur had the initial Strömberg radius fallen within the gradient. It is therefore likely that the perturbed density profile would prevent further growth of the instabilities until they approach the breakout radii found in our one-dimensional calculations discussed below. Accurate models of I-front transitions are therefore key to capturing the correct growth of instabilities and demand full radiation hydrodynamical treatment of the ionized flows.

If the Strömberg radius lies beyond the flat central core in the one-dimensional density profile of eq. 3 then its value is given by

$$R_\omega = R_S \left[\frac{3 - 2\omega}{3} + \frac{2\omega}{3} \left(\frac{r_c}{R_S} \right)^3 \right]^{1/(3-2\omega)} \left(\frac{R_S}{r_c} \right)^{2\omega/(3-2\omega)}, \quad (12)$$

where R_S is the Strömberg radius for the front in a uniform medium. If $R_\omega > r_c$ the I-front executes the classical transition to D-type but then soon reverts to R-type as it descends the gradient. The Franco *et al.* (1990) analyses do not address the evolution of the front when it is initially confined to the core ($R_S < r_c$), as in these models. To determine the outcome of the front in this regime we performed two sets of one-dimensional calculations in the density profile used earlier but without perturbations. We extended the outer boundary of the mesh to 20 pc with 2000 radial zones to preserve the spatial resolution. One set had a central photon rate $\dot{n}_{ph} = 1.0 \times 10^{48} \text{ s}^{-1}$ as before while $\dot{n}_{ph} = 5.0 \times 10^{49} \text{ s}^{-1}$ in the other set. This larger rate sets $R_\omega = 0.26 \text{ pc}$, outside the central plateau. One calculation in each set had a cutoff temperature of 1000 K while the other had a cutoff of 100 K; the background temperature in each was 100 K. The evolution of the front was followed for 1.3 Myr in the first set and for 45 kyr in the second set (much less time is required when there is rapid escape down the gradient). Flow profiles for all four calculations appear in Fig 6.

Even out to 20 pc, ten times the distance to which our earlier models were followed, the density and ionization fraction profiles in the left panel of Fig 6 reveal that the I-front remains trapped by the shock at the lower photon rates. The 100 K shell is only half as thick as the 1000 K shell but has ten times its density. The higher recombination rate in the cooler shell offsets its smaller width to confine the front. Note that radiative cooling in both cases lowers the shell to the cutoff temperature. When we extend the grid boundary to 200 pc at the

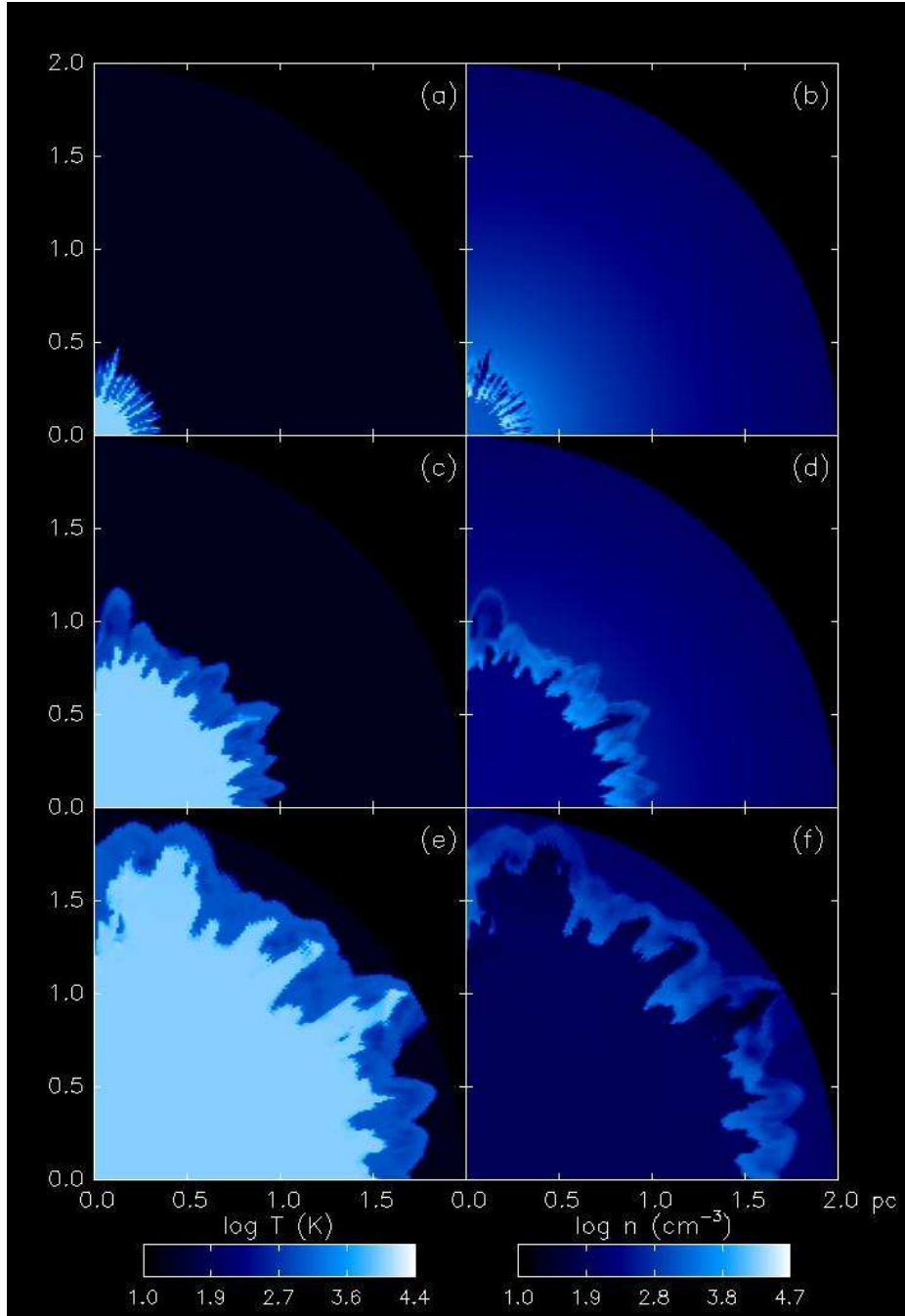


FIG. 4.— Dynamical instability in a D-type front propagating outward along an r^{-2} density gradient with metal line cooling, run S31. Panels (a), (c), and (e): temperature evolution at 20.8 kyr, 96.2 kyr, and 177.4 kyr. Panels (b), (d), and (f): density evolution at 20.8 kyr, 96.2 kyr, and 177.4.

same spatial resolution (thereby ensuring that the front remains on the grid for the 10 Myr lifetime of a star with these emission rates (Schaerer 2002)), we find that the front finally breaks through the 1000 K shell at 90 pc and through the 100 K shell at 64 pc. In these calculations the shock gains strength as it descends the density gradient. Line cooling still collapses gas into a relatively thin layer at the base of the shell but cannot cool all the material that accumulates as the shock accelerates so the shell heats and thickens. When the shell's outer layers reach 10,000 K, collisional ionizations assist the I-front

to break through the shock.

On the other hand, the right panel demonstrates that if $R_S = 0.26 \text{ pc} > r_c$, the front breaks free of the shock just past R_S as predicted by Franco *et al.* (1990). Reverting to R-type, the front quickly exits the spherical cloud, leaving behind a steepening ionized core shock at the site of detachment as seen in the density panel. Little gas dynamical evolution occurs over the time in which the front crosses the grid. The higher density of the cooler shell slightly delays I-front breakout (by $\sim 2 - 3$ kyr). This implied that instability growth would be

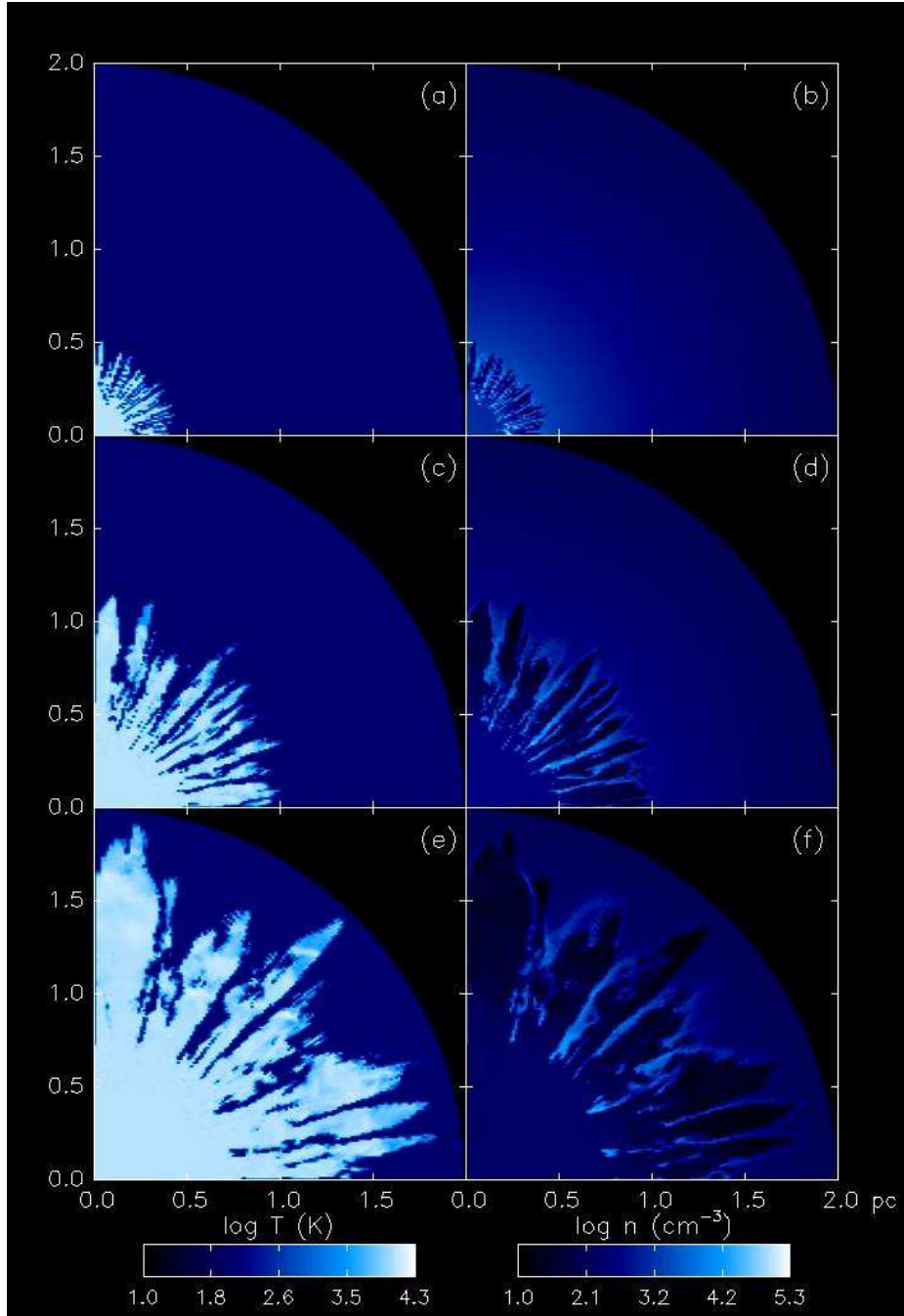


FIG. 5.— D-type ionization front instability in an r^{-2} density gradient with metal line cooling, run S22. Panels (a), (c), and (e): temperature evolution at 20.8 kyr, 67.9 kyr, and 124.5 kyr. Panels (b), (d), and (f): density evolution at 20.8 kyr, 67.9 kyr, and 124.5 kyr.

particularly explosive in cases where R_S lies beyond the core radius.

4.3. S31 Breakout Instability

To test this conjecture we devised a new S31 run with $\dot{n}_{ph} = 5.0 \times 10^{49} \text{ s}^{-1}$. We imposed random variations on the density as before but beyond radii of 0.29 pc in order to allow the I-front to become fully D-type at $R_\omega = 0.26$ pc before encountering the perturbations. Temperature and density images for $\phi = \pi/2$ in this calculation are shown in Fig (7) for 9.4, 13.2, and 15.1 kyr. Radiation

breakout through cracks in the shock rapidly ensues and the front erupts through the envelope in spikes which are R-type, as evidenced by the short escape times and the lack of hydrodynamic response in the ionized fingers. The slightly jagged edges in some of the spikes are artifacts of the spherical polar coordinate mapping to cartesian coordinates. Fragmentation of the shell is visible at early times as bright dots in the shell in the density panels but it soon disappears as the clumps are photoionized and then dispersed on time scales set by the sound speed in the postfront gas. The maximum density achieved in

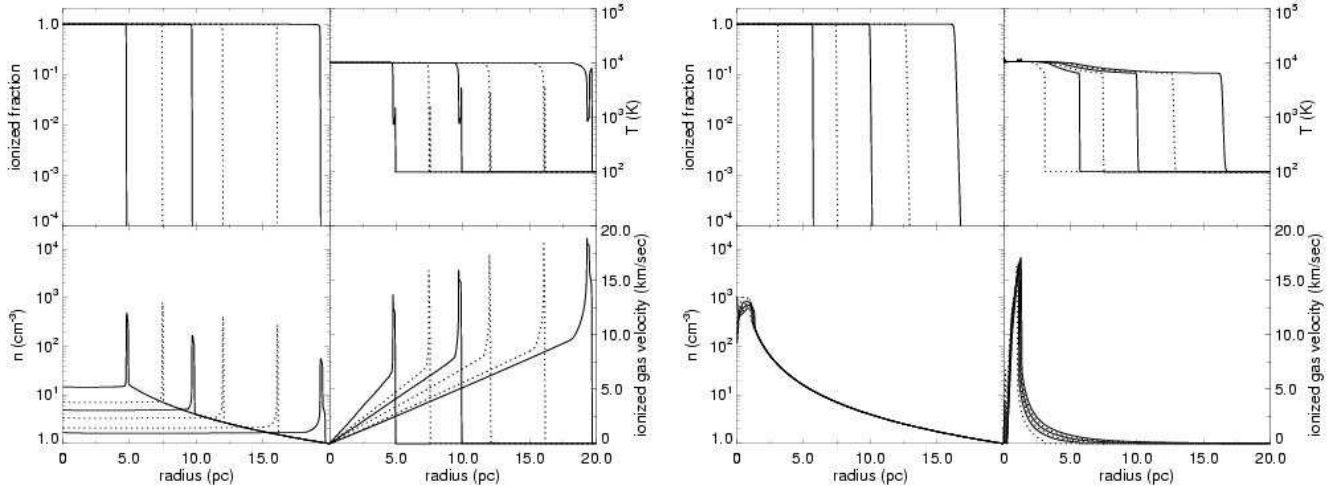


FIG. 6.— Hydrodynamical profiles for ionization fronts in a spherically-symmetric r^{-2} density stratification. Solid lines are I-front profiles with gas cooling truncated at 1000 K while dotted lines denote profiles in which gas cooling is halted below 100 K. Left panel: $R_S < r_c$. 1000 K profiles are at 0.48 Myr, 0.82 Myr, and 1.37 Myr while the 100 K profiles are at 0.7 Myr, 1.01 Myr, and 1.26 Myr. Right panel: $R_S > r_c$. 1000 K profiles are at 36 kyr, 40 kyr, and 44 kyr while the 100 K profiles are at 32 kyr, 38 kyr, and 42 kyr.

this simulation was $5.47 \times 10^4 \text{ cm}^{-3}$. The spikes remain fairly narrow because they elongate rapidly in comparison to hydrodynamical time scales, but they do begin to drive weak transverse shocks at their base as the ionized gas begins to laterally expand. These unstable modes do not fall in any of the categories discussed so far because they evolve as fast R-type structures.

5. R-TYPE SHADOW INSTABILITIES

In this test, a plane-parallel R-type ionization front enters the yz -face of a rectangular box with a uniform gas density except for a spherical bump slightly offset from the face of entry. The density in the bump varies linearly in radius from the ambient value at its center to either 50% below or above this value at its surface. Our simulation volume has a length of 1.0 pc along the x -axis and 0.25 pc along the y and z -axes, with 1000, 250, and 250 zones in the x , y , and z directions respectively. The gas number density in the box is 1000 cm^{-3} and is hydrogen only. The temperature of the gas was set to 72 K, yielding a sound speed c_s of 1 km/s. The fixed energy ϵ_I per photoionization was 0.8 eV to yield initial postfront temperatures of 10^4 . The incident photon flux along the x -axis at the entry face was $3.0 \times 10^{11} \text{ cm}^{-2} \text{ s}^{-1}$ to approximate that of an O star at its Strömgren radius. The radius of the perturbation was 0.0125 pc and was positioned 0.05 pc along the x -axis and centered in the yz -plane. Reflecting and outflow boundary conditions were applied at the 0 pc and 1.0 pc faces, respectively, with reflecting boundaries along the other four faces.

Our physical parameters for this test are similar to those of the two-dimensional simulations of Williams (1999), except for cooling. In those models near-isothermality was enforced by setting $\gamma = 1.1$ and the internal energy of the ionized gas to be constant to guarantee $c_s \sim 10 \text{ km/sec}$. In contrast, we applied the same cooling algorithm described earlier with a cutoff temperature of 1000 K. The front reaches a Strömgren distance

of 0.32 pc at approximately 1000 yr:

$$x_{Str} = \frac{F_0}{n^2 \alpha_B} \quad (13)$$

where F_0 is the photon flux ($\text{cm}^{-2} \text{ s}^{-1}$), n is the number density of neutral hydrogen and α_B is the case B recombination coefficient. The simulation volume was partitioned into 25 uniform tiles, with five divisions along both the y -axis and z -axis and each tile spanning the length of the volume in the x direction.

We show xy slices at $z = 0$ of the temperature and density evolution of the shadowing instability in Figs 8 and 9 due to an underdense perturbation at 1.9 kyr, 4.9 kyr, and 12.6 kyr. At 1.9 kyr the front has transitioned to D-type and the original corrugation in the R-type front is well into the nonlinear growth phase. The expanding photoevaporated perturbation is faintly visible on the left of the figure. The twin peaks in the instability are xy slices through a ringed jet that is due to the radial density profile of the spherical bump: the R-type front preferentially advances along the lines of sight parallel to the x -axis that cut the underdense regions close to the surface of the bump. Along the line of sight piercing the bump through its center, the front advances at nearly the same rate as in the unperturbed medium because the densities along this path through the bump are close to those in the surrounding gas.

At later times cooling in the shell fractures the instability into multiple jets with highly nonlinear growth and morphologies reminiscent of the density structures visible in the two-dimensional numerical experiments. No temperature images of the 1999 work are available so it is not possible to directly compare the distribution of ionized and shocked gas within the jets or verify the existence of the ionized extensions into the shock that are present in our models. The unperturbed regions of the front snowplow gas into a somewhat broader shell than in the Williams (1999) models because the gas can only cool to 1000 K. The length of the jet in our model (0.14

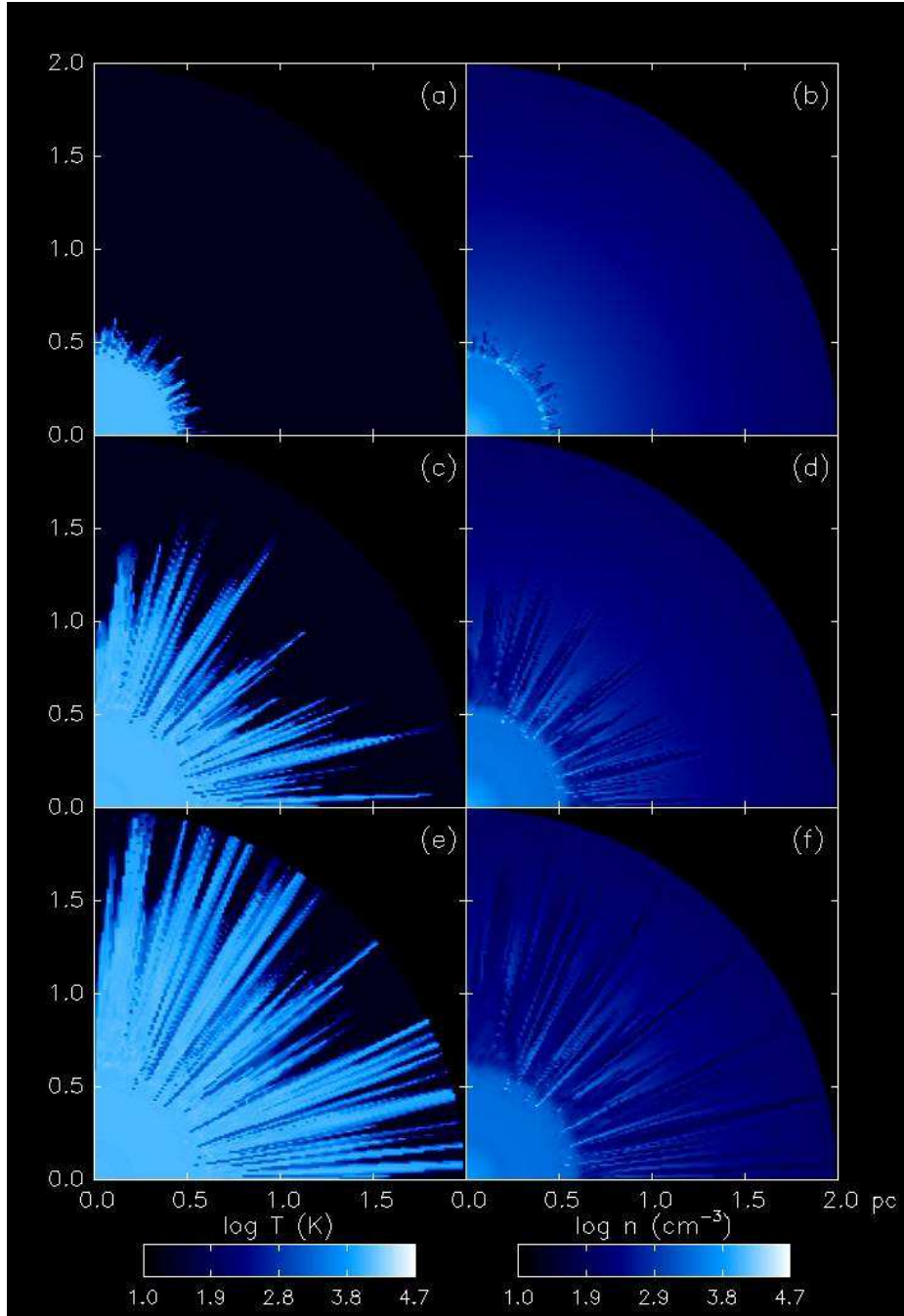


FIG. 7.— Run S31 with $R_\omega > r_c$. Panels (a), (c), and (e): temperature evolution at 9.4, 13.2, and 15.1 kyr. Panels (b), (d), and (f): density evolution at 9.4, 13.2, and 15.1 kyr.

pc) is somewhat shorter than in the Williams runs due in part to the lower ionizing flux. However, intrinsic differences between two and three-dimensional flows may also come into play, as the additional degree of freedom opens transverse flow channels that may quench the instability. Indeed, some vorticity is evident in the flow at later times, a possible signature that instability growth is coupling to turbulent motion in the gas and being reduced. The densities in the jets range from 19.0 cm^{-3} to $3.72 \times 10^4 \text{ cm}^{-3}$, a factor of 4 or 5 lower than in the 1999 experiments. The greater maxima in the earlier

work in part arise from the higher density jumps permitted across the isothermal shocks in those models as well as from the lower temperatures to which the postshock gas can cool. As the central jet advances it widens as ionized gas in its interior expands perpendicular to the flow.

Two features also worth mention are the density knots in the shock located above and below the midplane of the jets at their base at 1.9 kyr. As the front advances, radiation escapes past the knots and forms jets that migrate across the face of the shock as they elongate. Shortly

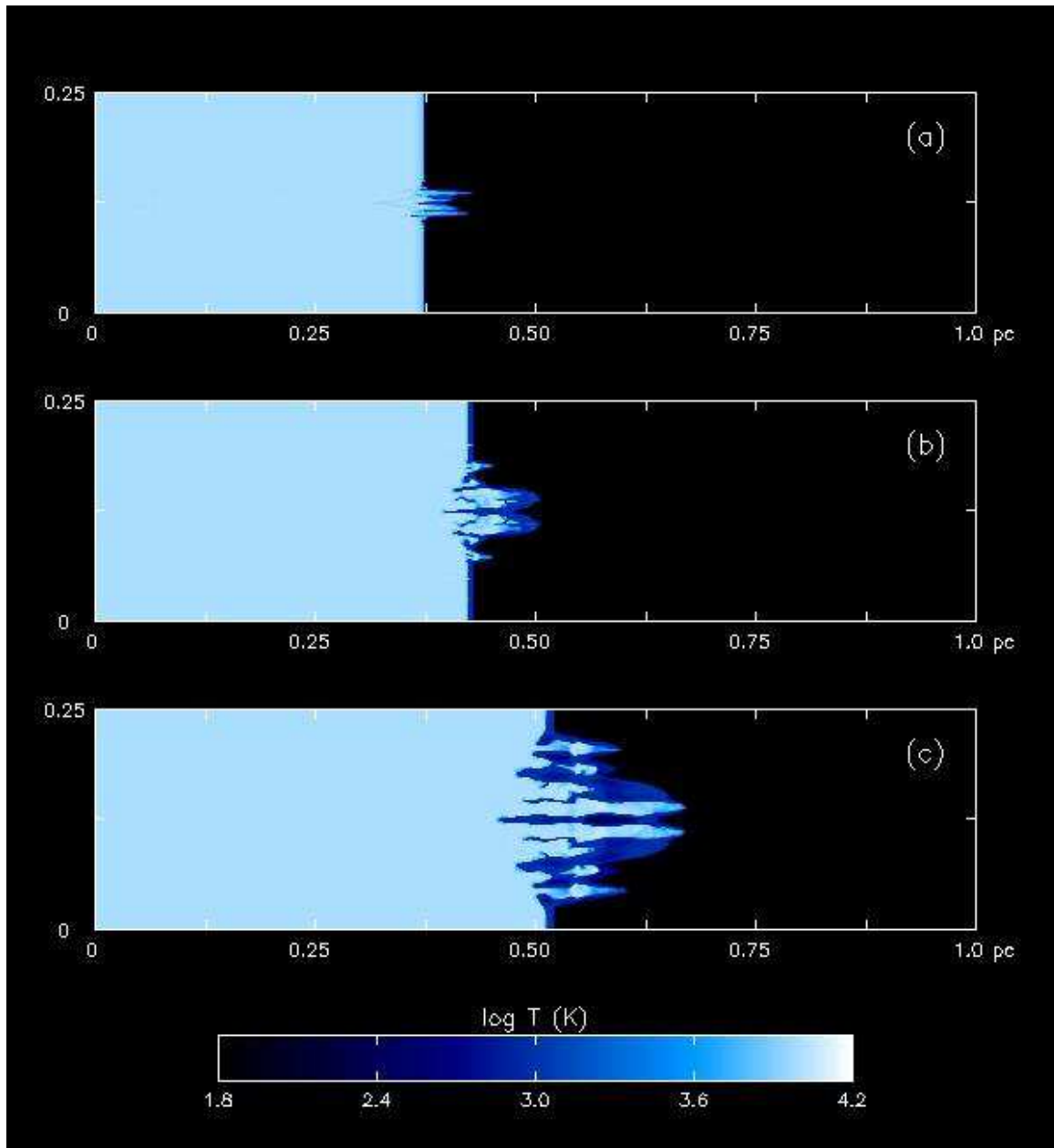


FIG. 8.— Temperature evolution of an I-front shadow instability due to an underdense spherical underdensity: (a) 1.9 kyr, (b) 4.9 kyr, and (c) 12.6 kyr.

thereafter, smaller disturbances in the shock materialize further from the base of the central jet, possibly triggered by acoustic waves along the shock or perhaps merely numerical artifacts. These density fluctuations quickly cool and create cracks in the shock through which ionizing photons penetrate, forming smaller subsidiary jets that later merge with the widening central jet in complicated hydrodynamical flows. The original knots are present in the two-dimensional runs and are attributed by Williams to a type of zero-wavelength odd-even numerical instability (zero-wavelength in the sense that it would be manifest at all resolutions). The phenomena apparently arise because the I-front itself is not resolved by the grid. Just as postshock oscillations can come to dominate shocked

flow not broadened by a few zones with artificial viscosity in lower-order hydrodynamical schemes, under certain circumstances sharp I-fronts can preferentially advance in an oscillatory fashion across adjacent zones. Williams removed this effect in his simulations by setting the photoionization cross section to be a function of zone width (in direct analogy to artificial viscosity), hence broadening the front. Practical applications employing multifrequency radiative transfer (for Population III stellar and miniquasar hard spectra) may obviate this feature because the spread in photon mean free paths would naturally widen I-fronts in many environments without recourse to artificial means.

6. CONCLUSION

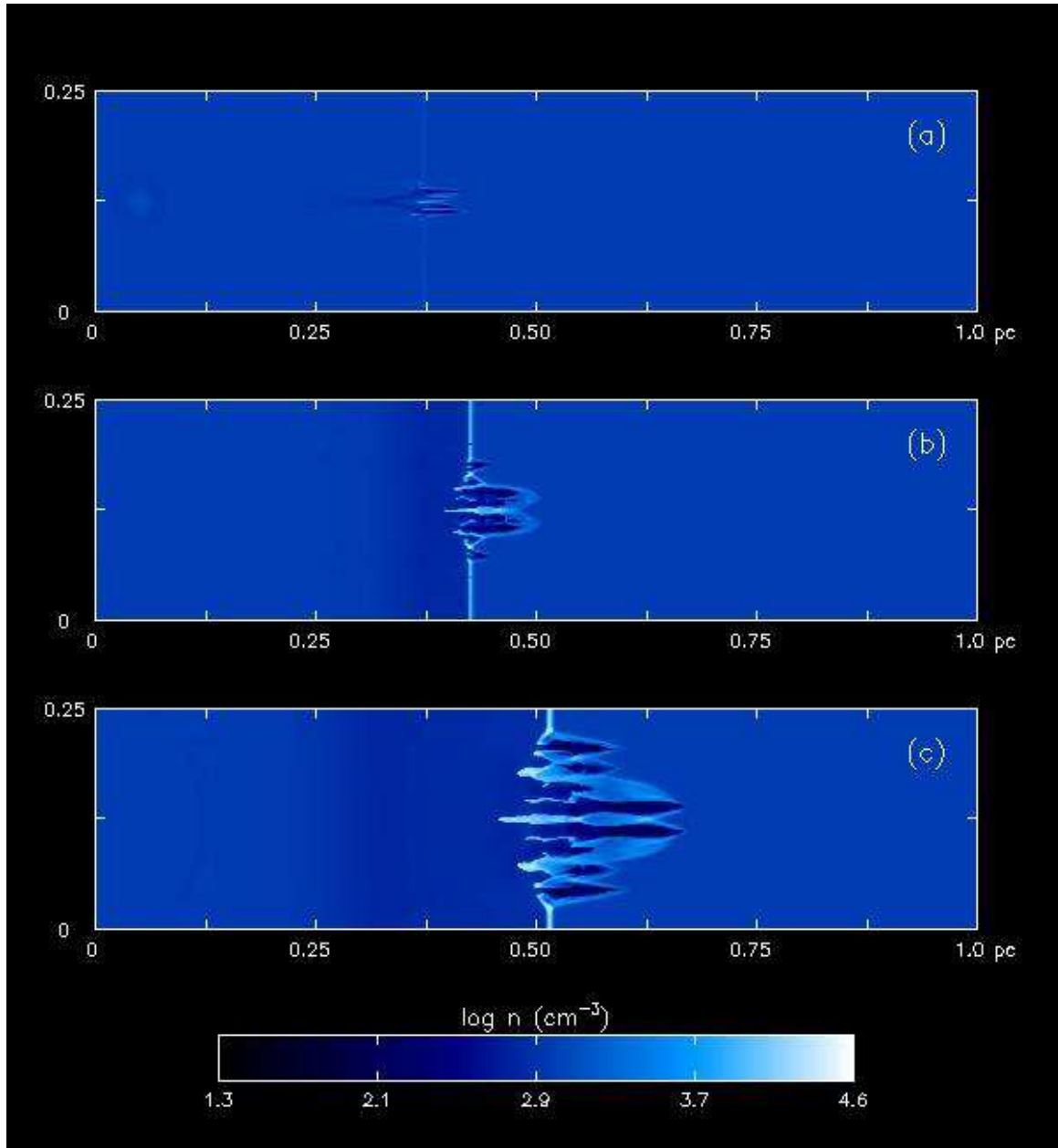


FIG. 9.— Density evolution of an I-front shadow instability due to the spherical underdensity: (a) 1.9 kyr, (b) 4.9 kyr, and (c) 12.6 kyr.

For the past ten years, the general paradigm of ionization front instabilities in the ISM has been one of sword-like structures with unrestrained amplitude growth in a wide variety of environments. Our new models temper this view with saturated modes that likely drive turbulent flows in some instances. The morphology of the S31 instability in particular suggests that some modes may efficiently drive turbulence in the shocked shell, with possible implications for time scales of subsequent star formation in the region. The numerous short-wavelength ionized spikes in the shock at early times later gather into fewer long-wavelength structures, so energy is transported at first from smaller scales to larger ones by the flow. Later, these large scale flows crumple into ever smaller scales as the saturated instabilities devolve into

shear motions and develop the vorticity evident in the Kelvin-Helmholtz features appearing in panel (f) of Fig 4. We expect this process to be more prominent in actual molecular clouds because the r^{-2} profile of a core truncates in relatively high intra-cloud densities that would further flatten the instabilities. While our current mesh can resolve the shell breakup and ionized fingers well, these features would have to be evolved for longer times on finer grids able to capture turbulent cascades to determine the extent to which turbulence arises in the cloud. Nevertheless, the possibility that ionization front instabilities together with winds from massive stars and supernova explosions may provide an important source of turbulent support in star forming clouds in the galaxy today is an intriguing one.

We find that the dimensionality of our models distinguishes them from previous work more than their improved physics. The structures emerging in our simulations bear resemblance to many objects visible in the ISM today. The globules and pillars in the S31 run are reminiscent of those seen in the Eagle nebula while the long wispy extensions in the S22 run are comparable to those in many planetary nebula such as NGC 6751. The clumping that is prevalent in the galaxy is also evident in our models. In reality, ionization front instabilities compete with wind-blown structures and blast waves to produce the panoply of features in the local interstellar medium. How all three act in concert to create the circumstellar environments of massive stars and gamma-ray bursts is an important question to be addressed in future work. Likewise, how H II region instabilities interact with the magnetic fields threading molecular clouds remains poorly understood. We expect that unstable modes will not be seriously suppressed on parsec scales because of the relative magnitudes of ionized gas and magnetic field pressures, but their evolution could be altered on larger scales as they approach pressure equilibrium with their surroundings.

A question of relevance to cosmological reionization is whether I-front instabilities arise in the primordial clouds of primeval massive stars and protogalaxies. In pristine gas shocks must resort to atomic hydrogen line cooling and Compton cooling at high redshifts, which are far less efficient processes than metal line emission. If the shocked flows are non-radiating, no Vishniac instabilities can develop or be amplified by radiation so the fronts would be stable. On the other hand, I-front shocks accelerate if they emerge from cosmological minihalos with density gradients steeper than r^{-2} . Their exit may thus be subject to Rayleigh-Taylor instabilities that ionizing radiation could blossom into much larger structures. We further note that hard Population III or miniquasar UV and x-ray spectra can significantly broaden comological I-fronts, and it is unclear what impact the layer of partial ionization will have on instability formation. These ques-

tions together with how I-fronts sculpt gas clouds in the early intergalactic medium will be the focus of studies to come.

Finally, we caution that all our models adopted the on-the-spot approximation, in which recombination photons are assumed to be reabsorbed in their zone of origin before escaping. In reality, reprocessed radiation isotropically emitted within the ionized fingers may halt their growth by eroding them from within. Recombination radiation is believed to dominate the photon budget in the outer radii of centrally concentrated H II regions like those examined in our study (Ritzerveld 2005). Direct transport of diffuse ionizing radiation exhausts current ray tracing techniques, so the implementation of flux-limited diffusion for recombination photons in ZEUS-MP is currently underway in order to study their influence on instabilities in future models. Nevertheless, we expect that diffuse radiation will at most blunt the instabilities, not prevent their formation or destroy them because the fragmentation of the shell and breakout of the radiation through the cracks is a very robust feature of the fronts.

We thank the anonymous referee, whose insightful critique significantly improved the quality of this paper. DW is grateful for useful discussions concerning this work with Guillermo Garcia-Segura, Alex Heger, Mordecai-Mark Mac Low and Marcelo Alvarez, as well as for conversations with Hajime Susa and Naoki Yoshida at the University of Washington INT workshop “The First Stars and Evolution of the Early Universe” held from June 19 to July 21, 2006. He also thanks Brian O’Shea for his software package for mapping the spherical polar coordinate data in this study onto cartesian grids for the images in this paper. This work was carried out under the auspices of the National Nuclear Security Administration of the U.S. Department of Energy at Los Alamos National Laboratory under Contract No. DE-AC52-06NA25396. The simulations were performed at SDSC and NCSA under NRAC allocation MCA98N020.

REFERENCES

- Arquilla, R., & Goldsmith, P. F. 1985, *ApJ*, 297, 436
 Axford, W. I. 1964, *ApJ*, 140, 112
 Bertoldi, F. 1989, *ApJ*, 346, 735
 Brand, P. W. J. L. 1981, *MNRAS*, 197, 217
 Canto, J., Raga, A., Steffen, W., & Shapiro, P. 1998, *ApJ*, 502, 695
 Capriotti, E. R. 1973, *ApJ*, 179, 495
 Dale, J. E., Bonnell, I. A., & Whitworth, A. P. 2007, *MNRAS*, 42
 Dalgarno, A. & McCray, R. A. 1972, *ARA&A*, 10, 375
 Franco, J., Diaz-Miller, R. L., Freyer, T., & Garcia-Segura, C. 1998, *ASP Conf. Ser. 141: Astrophysics From Antarctica*, 141, 154
 Franco, J., Tenorio-Tagle, G., & Bodenheimer, P. 1990, *ApJ*, 349, 126
 Freyer, T., Hensler, G., & Yorke, H. W. 2003, *ApJ*, 594, 888
 Frieman, E. A. 1954, *ApJ*, 120, 18
 Fuller, T. M. & Couchman, H. M. P. 2000, *ApJ*, 544, 6
 Garcia-Segura, G., & Franco, J. 1996, *ApJ*, 469, 171
 Giuliani, J. L. 1979, *ApJ*, 233, 280
 Gregorio Hetem, J. C., Sanzovo, G. C., & Lepine, J. R. D. 1988, *A&AS*, 76, 347
 Hayes, J. C., Norman, M. L., Fiedler, R. A., Bordener, J. O., Li, P. S., Clark, S. E., ud-Doula, A., Mac Low, M. -M., astro-ph/0511545.
 Kahn, F. D. 1958, *Reviews of Modern Physics*, 30, 1058
 Mac Low, M.-M., & Norman, M. L. 1993, *ApJ*, 407, 207
 Mellema, G., Raga, A. C., Canto, J., Lundqvist, P., Balick, B., Steffen, W., & Noriega-Crespo, A. 1998, *A&A*, 331, 335
 Mizuta, A., Kane, J. O., Pound, M. W., Remington, B. A., Ryutov, D. D., & Takabe, H. 2005, *ApJ*, 621, 803
 Mizuta, A., Kane, J. O., Pound, M. W., Remington, B. A., Ryutov, D. D., & Takabe, H. 2006, *ApJ*, 647, 1151
 Newman, R. C., & Axford, W. I. 1967, *ApJ*, 149, 571
 Osterbrock, D. *Astrophysics of Gaseous Nebulae and Active Galactic Nuclei*, University Science Books 1989.
 Ritzerveld, J. 2005, *A&A*, 439, L23
 Schaerer, D. 2002, *A&A*, 382, 28
 Shapiro, P. R., Iliev, I. T., & Raga, A. C. 2004, *MNRAS*, 348, 753
 Soker, N. 1998, *MNRAS*, 299, 562
 Spitzer, L. J. 1954, *ApJ*, 120, 1
 Sysoev, N. E. 1997, *Astronomy Letters*, 23, 409
 Vandervoort, P. O. 1962, *ApJ*, 135, 212
 Vishniac, E. T. 1983, *ApJ*, 274, 152
 Whalen, D., Abel, T., & Norman, M. L. 2004, *ApJ*, 610, 14
 Whalen, D., & Norman, M. L. 2006, *ApJS*, 162, 281
 Williams, R. J. R. 1999, *MNRAS*, 310, 789
 Williams, R. J. R. 2002, *MNRAS*, 331, 693
 Williams, R. J. R., Dyson, J. E., & Hartquist, T. W. 2000, *MNRAS*, 314, 315

Yoshida, N., Oh, S. P., Kitayama, T., & Hernquist, L. 2006,
astro-ph/0610819